International Journal of Solids and Structures 51 (2014) 4026–4037

Contents lists available at ScienceDirect

International Journal of Solids and Structures

journal homepage: www.elsevier.com/locate/ijsolstr

Stretchability and compliance of freestanding serpentine-shaped ribbons

Thomas Widlund [a,b], Shixuan Yang [a], Yung-Yu Hsu [c], Nanshu Lu [a,*]

[a] Center for Mechanics of Solids, Structures and Materials, Department of Aerospace Engineering and Engineering Mechanics, University of Texas at Austin, Austin, TX 78712, USA
[b] Arts et Métiers Paristech Engineering School, 51006 Châlons-en-Champagne, France
[c] MC10 Inc., 36 Cameron Avenue, Cambridge, MA 02140, USA

ARTICLE INFO

Article history:
Received 6 January 2014
Received in revised form 5 June 2014
Available online 5 August 2014

Keywords:
Serpentine
Stretchability
Stiffness
Curved beam theory

ABSTRACT

High-performance stretchable electronics have to utilize high-quality inorganic electronic materials such as silicon, oxide or nitride dielectrics, and metals. These inorganic materials usually crack or yield at very small intrinsic strains, for example, 1%, whereas bio-integrated electronics are expected to at least match the stretchability of bio-tissues (20%) and deployable structure health monitoring networks are expected to expand from wafer scale (several centimeters) to cover macroscopic structures (several meters). To minimize strains in inorganic materials under large deformation, metallic and ceramic films can be patterned into serpentine-shaped ribbons. When the ribbon is stretched, some sections of the ribbon can rotate and/or buckle to accommodate the applied displacement, leaving much smaller intrinsic strain in the materials compared to the applied strain. The choice of the shape of the serpentine depends on systematic studies of the geometric variables. This paper investigates the effect of serpentine shapes on their stretchability and compliance through theoretical, numerical, and experimental means. Our closed-form curved beam solutions, FEM results, and experimental measurements have found good agreement with one another. Our results conclude that in general, the narrower ribbon, the larger arc radius and arc angle, and the longer arm length will yield lower intrinsic strain and effective stiffness. When the arm length approaches infinite, the stretchability can be enhanced by several orders. A few unexpected behaviors are found at arc angles that are close to straight bars. With additional practical constraints such as minimum ribbon width and finite overall breadth, the optimal serpentine shape can be accurately determined using our closed-form analytical solution.

1. Introduction

In recent years, stretchable electronics start to find exciting applications in wearable electronics, smart surgical tools, compliant power sources, as summarized in four recent review articles (Kim et al., 2012a,b,c; Lu and Kim, 2013). Examples include epidermal electronics for vital-sign monitoring (Kim et al., 2011; Huang et al., 2012; Yeo et al., 2013), fingertip electrotactile actuators for smart surgical gloves (Ying et al., 2012), instrumented balloon catheters for minimally invasive surgeries (Kim et al., 2011), multifunctional cardiac webs (Kim et al., 2012), and stretchable batteries (Xu et al., 2013). A fundamental challenge of stretchable electronics is to build a mechanically compliant system which is able to deform drastically without affecting its electrical functionalities. High-performance stretchable electronics have to utilize high-quality, inorganic electronic materials such as silicon, gold, and oxides or nitrides, which are known to be very stiff and even brittle materials. For example, thin films of ceramic materials such as silicon, oxides, and nitrides tend to rupture at very small strains, around 1% (Leterrier et al., 1997; Gleskova et al., 1999; Sun et al., 2012). Although copper thin films well bonded to polyimide substrates have been stretched beyond 50% without fracture (Lu et al., 2007), most of the deformation is plastic and therefore, irreversible. The elastic regime of metal deformation is still limited to 1% or less (Hommel and Kraft, 2001). To minimize strains in metal interconnects under large deformation, either out-of-plane sinusoidal nanoribbons/nanomembranes (Lacour et al., 2005; Khang et al., 2006) or in-plane serpentines (Gray et al., 2004; Kim et al., 2008) are employed to replace straight wires. Comparing the two popular strategies, in-plane serpentines are more fabrication and integration friendly because no pre-stretch of the rubber substrate is required and low profile is preserved. In fact, not only metals but also silicon and two-dimensional graphene can be patterned into

* Corresponding author. Tel.: +1 512 471 4208.
E-mail address: nanshulu@utexas.edu (N. Lu).

http://dx.doi.org/10.1016/j.ijsolstr.2014.07.025
0020-7683/

serpentine ribbons to achieve high stretchability (Kim et al., 2011, 2008, 2011; Zhu et al., 2014). Recently developed micro-transfer-printing techniques (Meitl et al., 2006) has enabled the integration of well-patterned inorganic films and ribbons on elastomer substrates. When the substrate is stretched, serpentine ribbons can rotate in plane and buckle out of plane to accommodate the applied deformation, resulting in greatly reduced intrinsic strains in the inorganic materials as well as minimized stiffness at the system level. Low system-level effective stiffness is critical for bio-integration because devices as compliant as bio-tissues can conform to and deform together with the bio-tissue without detachment or imposing any significant mechanical constraint (Kim et al., 2011; Huang et al., 2012; Yeo et al., 2013).

Besides stretchable electronics, serpentine structures can also be found in a lot of expandable systems made out of intrinsically stiff materials. Examples include the cardiovascular stents for angioplasty (Beyar et al., 1997) or percutaneous coronary intervention (Roguin et al., 1997), and deployable sensor networks for structural health monitoring (Lanzara et al., 2010). Tubular metallic stents in the form of a serpentine-meshed scanfold can be inserted into blood vessels in a very small initial diameter, tunnel through the veins and arteries, and get expanded by more than 200% using a balloon catheter, to provide support inside the patient's arteries. As another example, ultra narrow, highly tortuous serpentines were incorporated in the design of a spider-web-like highly expandable sensor network (Lanzara et al., 2010). The microfabrication of inorganic-material-based sensors which has to utilize regular-sized spinners, mask aligners, and vacuum chambers can all be performed on a wafer-sized rigid substrate. Once the circuit is released from the rigid substrate, the sensor network can be deployed by more than 100 times in area so that they can cover macroscopic civil or aerospace structures to perform structure health monitoring. In both examples, the large expandability comes from just the in-plane rigid body rotation of the freestanding serpentine ligaments.

Although serpentines have been widely used as the stretchable configuration of stiff materials, the designs of the serpentine shape are still largely empirical. According to existing studies, the applied strain-to-rupture of metallic serpentine ribbons varies from 54% to 1600%, depending on the geometric parameters such as ribbon width, arc radius, arm length, substrate support, and so on (Gray et al., 2004; Kim et al., 2008; Lanzara et al., 2010; Hsu et al., 2009; Brosteaux et al., 2007; Xu et al., 2013). A few experimental and finite element modeling (FEM) studies have been conducted to provide insights into the shape-dependent mechanical behavior (Gray et al., 2004; Hsu et al., 2009; Li et al., 2005) of serpentine ribbons. Two recent theoretical articles provided viable routes to predict the stretchability of buckled serpentines (Zhang et al., 2013a) and self-similar serpentines (Zhang et al., 2013b), but the shapes of the unit cells are very limited. Moreover, the effective compliance of the serpentine structure and the shape optimization under practical constraints have been rarely discussed. This paper performs analytical, FEM, and experimental studies on freestanding serpentines with three systematically varied dimensionless geometric parameters. The closed-form plane strain solution can be applied to predict the stretchability and effective stiffness of numerous serpentine structures. The analytical solution can also be used to optimize the three dimensionless geometric parameters under one optimization goal – maximum stretchability, and two practical constraints – e.g. no material overlap and finite breath of the structure at a given ribbon width resolution.

This paper is organized as follows. Section 2 summarizes the analytical, FEM, and experimental approaches we use. Section 3 compares the analytical, FEM, and experimental results for systematically varied serpentine shapes. Section 4 demonstrates how to determine the optimal serpentine shape under certain practical constraints using the analytical solutions. Concluding remarks are provided in Section 5. In Appendix A, derivations based on elasticity theory (i.e. Airy's function) are provided. Appendix B derives the load–displacement relation using Castigliano's method (i.e. energy method) and the strain distribution using the Winkler curved beam (CB) theories.

2. Analytical, fem, and experimental approaches

It has been observed that when freestanding serpentine ribbons have large width-to-thickness ratio, they tend to buckle out-of-plane when subjected to end tensile displacements (Kim et al., 2011, 2008; Li et al., 2005) whereas when their width-to-thickness ratios are small, the deformation is completely in plane (Lanzara et al., 2010). Although general three-dimensional (3D) theories for curved thin rods are available (Love, 2011), out-of-plane buckling and post-buckling analysis for curved beams only yields analytical solutions for very limited shapes and loading conditions (Kang and Yoo, 1994). To initiate the theoretical analysis and optimization of free standing serpentine ribbons, we start with a two dimensional (2D) plane strain model, which suppresses the out-of-plane buckling deformation. A unit cell cut out of a one-directional periodic serpentine ribbon is depicted in Fig. 1A. The unit cell of a so-called "horseshoe" serpentine is composed of an arc joined end to end with its upside-down mirror image. Based on the conventional horseshoe shape, we add a linear "arm" section between the two arcs. The unit cell of this generic serpentine can be well defined by four geometric parameters: the ribbon width w, the arc radius R, the arc angle α, and the arm length l. The ribbon thickness t is assumed to be unit in the plane strain model. Hence the end-to-end distance S of a unit cell can be expressed by

$$S = 4\left(R\cos\alpha - \frac{l}{2}\sin\alpha\right) \tag{1}$$

When this unit cell is subjected to a tensile displacement u_0 at each end, the effective applied strain ε_{app} is defined as

$$\varepsilon_{app} = \frac{2u_0}{S} \tag{2}$$

Therefore a straight ribbon (i.e. $\alpha = -90°$) of length S should have a uniform strain of ε_{app} if the end effects are neglected. Attributing to symmetry and anti-symmetry, a unit cell can ultimately be represented by a quarter cell with fixed boundary at the axis of symmetry and a displacement of $u_0/2$ at the end, as shown in Fig. 1B. The reaction force is named P in Fig. 1B. The end of the unit cell is considered free to rotate because we assume it is a unit cell cut out of a long, periodic serpentine ribbon whose boundary conditions (i.e. whether clamped or simply-supported) do not affect the unit cell.

In this problem, two mechanical behaviors of serpentines are of particular interest to us: the stretchability and the effective stiffness. *Stretchability* is defined as the critical applied strain beyond which the material of the serpentine ribbon will rupture and will be denoted by ε_{app}^{cr}. Therefore, if the failure criterion $\varepsilon_{max} = \varepsilon_{cr}$ is adopted, where ε_{max} and ε_{cr} represent the maximum tensile strain and the intrinsic strain-to-rupture of the material, respectively, the normalized maximum tensile strain in the serpentine, $\varepsilon_{max}/\varepsilon_{app}$, will govern the stretchability by

$$\varepsilon_{app}^{cr} = \frac{\varepsilon_{cr}}{\frac{\varepsilon_{max}}{\varepsilon_{app}}} \tag{4}$$

Effective stiffness is defined as the ratio between the reaction force P and the effective displacement, $2u_0$. With Young's modulus E and Poisson's ratio ν, the stiffness of a plane strain straight ribbon

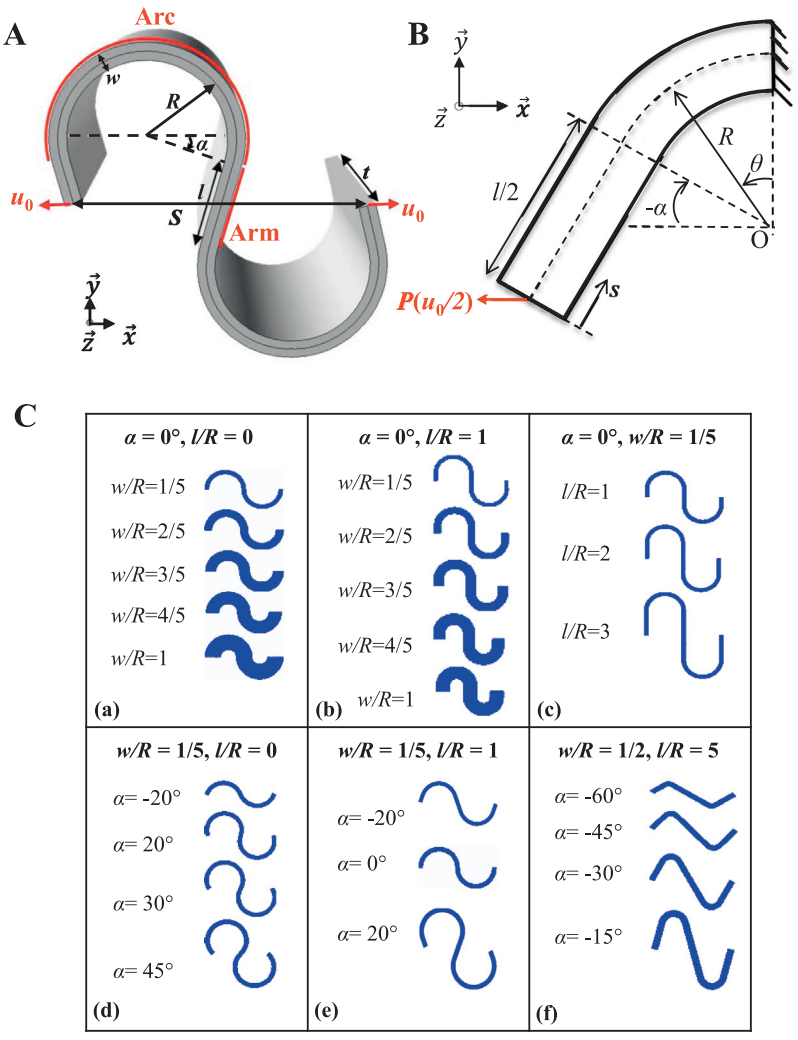

Fig. 1. (A) Schematics of a serpentine unit cell where R is the radius of the arc median line, w is the width, α is the arc angle, l is the arm length, and S is the end-to-end distance of the unit cell. The ribbon thickness t is assumed to be unit in the plane strain model. The unit cell is subjected to a tensile displacement of u_0 at each end. (B) Schematics of a quarter of a 2D plane strain unit cell with boundary conditions. θ is the angular variable for the arc section and s is the linear variable for the arm section. P is the reaction force as a result of an applied displacement of $u_0/2$. (C) Schematics of systematically varied serpentine shapes where (a) $\alpha = 0°$, $l/R = 0$, w/R varies; (b) $\alpha = 0°$, $l/R = 1$, w/R varies; (c) $\alpha = 0°$, $w/R = 5$, l/R varies; (d) $w/R = 1/5$, $l/R = 0$, α varies; (e) $w/R = 1/5$, $l/R = 1$, α varies, and (f) $w/R = 1/2$, $l/R = 5$, α varies.

of length S and width w is given by $\bar{E}w/S$, where $\bar{E} = E/(1-\nu^2)$ is the plane strain modulus. Therefore the effective stiffness of a serpentine ribbon normalized by that of straight ribbon of the same end-to-end length is given by $PS/(2\bar{E}wu_0)$. When α approaches $-90°$, i.e. when serpentine degenerates to linear ribbon, normalized effective stiffness should approach 1. Through dimensional analysis, the first objective of this paper is to derive the functional forms of

$$\frac{PS}{2\bar{E}wu_0} = f\left(\alpha, \frac{w}{R}, \frac{l}{R}\right) \tag{5}$$

and

$$\frac{\varepsilon_{max}}{\varepsilon_{app}} = g\left(\alpha, \frac{w}{R}, \frac{l}{R}\right) \tag{6}$$

which will be generic functions for all kinds of linear elastic materials. Functional forms of Eqs. (5) and (6) will be obtained from analytical and finite element methods. By varying α, w/R, and l/R systematically, various serpentine shapes can be achieved as depicted in Fig. 1C. Since dimensionless variables are used, self-similar serpentines, no matter macro-, micro-, or nano-scale, as long as their α, w/R, and l/R are all the same, their normalized effective stiffness and stretchability will not have any difference, assuming no size-dependent material properties.

Plane strain elasticity theory (e.g. Airy's function) and Winkler curved beam (CB) theories can both be directly applied to analyze the problem defined in Fig. 1B. Airy's function gives the most accurate solution even when w/R is close to 1, but CB theory offers closed form analytical solutions for serpentines with arbitrary α, w/R, and l/R. Results from CB theory agrees well with elasticity theory up to $w/R \leqslant 1/2$ (Bickford, 1998), which is within the range of interest. As a demonstration, we have applied Airy's function to find solutions to Eqs. (5) and (6) of a simple horseshoe unit cell with $\alpha = 0°$, $l/R = 0$, and varying w/R, as derived in Appendix A. Except for this example, analytical results obtained in the rest of the paper are derived using CB theories, with details provided in Appendix B.

Since the problem we analyze has a prescribed displacement boundary condition (Fig. 1A), to perform strain analysis, we first need to figure out the load–displacement relation for generic serpentine shapes using the schematics provided in Fig. 1B. In Appendix B, Castigliano's energy method has been applied to find out the load–displacement relation as follows:

$$\frac{PS}{2\bar{E}wu_0}=\frac{\frac{w}{R}\left(\cos\alpha-\frac{l}{2R}\sin\alpha\right)}{2\left[\begin{array}{c}\cos^2\alpha\left(\frac{l^3}{2R^3}+3\left(\frac{\pi}{2}+\alpha\right)\frac{l^2}{R^2}+12\frac{l}{R}-12\left(\frac{\pi}{2}+\alpha\right)\right)\\+\sin 2\alpha\left(6\left(\frac{\pi}{2}+\alpha\right)\frac{l}{R}+9\right)\\+\frac{w^2}{R}\left[\left(\frac{\pi}{2}+\alpha\right)\left(\frac{l}{2R}\cos\alpha+\sin\alpha\right)^2+\frac{l}{2R}\left(\sin\alpha+\frac{3\bar{E}}{2G}\cos\alpha\right)\right]+18\left(\frac{\pi}{2}+\alpha\right)\end{array}\right]} \tag{7}$$

which is also the expression for the normalized effective stiffness, as proposed before. It is obvious to conclude from Eq. (7) that the effective stiffness decreases monotonically with the minimization of w/R and the enhancement of l/R whereas the effect of α is not as straightforward.

Combining Eq. (7) with the equilibrium equations in Appendix B, the functional form of Eq. (6) is found to be:

$$\frac{\varepsilon_{max}}{\varepsilon_{app}}=\frac{\frac{w}{R}\left[\frac{12}{2-\frac{w}{R}}+\left(\frac{12}{2-\frac{w}{R}}-\frac{w}{R}\right)\left(\sin\alpha+\frac{l}{2R}\cos\alpha\right)\right]\left(\cos\alpha-\frac{l}{2R}\sin\alpha\right)}{\left[\begin{array}{c}\cos^2\alpha\left(\frac{l^3}{2R^3}+3\left(\frac{\pi}{2}+\alpha\right)\frac{l^2}{R^2}+12\frac{l}{R}-12\left(\frac{\pi}{2}+\alpha\right)\right)\\+\sin 2\alpha\left(6\left(\frac{\pi}{2}+\alpha\right)\frac{l}{R}+9\right)\\+\frac{w^2}{R}\left[\left(\frac{\pi}{2}+\alpha\right)\left(\frac{l}{2R}\cos\alpha+\sin\alpha\right)^2+\frac{l}{2R}\left(\sin\alpha+\frac{3\bar{E}}{2G}\cos\alpha\right)\right]+18\left(\frac{\pi}{2}+\alpha\right)\end{array}\right]} \tag{8}$$

It is not easy to tell the effect of the three different variables by just examining Eq. (8). So we will later plot this equation in comparison with FEM and experimental results in Section 3.

Commercial FEM package ABAQUS 6.10 is used to perform plane strain modeling of a unit cell as shown in Fig. 1A. The serpentine material is assumed to be linear elastic, with Young's modulus E = 130 GPa, and Poisson's ratio ν = 0.27 (e.g. silicon). Symmetric displacement boundary conditions are applied at both ends to ensure ε_{app} = 10% for all the models. Small deformation (i.e. linear geometric relation) is assumed. After convergence test, element size is always maintained to be smaller than $w/40$. Strain distribution and reaction force can be directly output from FEM. Note that although we have to specify E, ν and ε_{app} to perform FEM, the normalized results FEM results shown in Section 3 are independent of those inputs.

Experimental validation of the analytical and FEM approaches is conducted with 3D-printed acrylonitrile butadiene styrene (ABS) straight and serpentine ribbons. Instron Dual Column Testing System (Model 3367) and Bluehill 2 are used as the uniaxial tension test and data acquisition system. Displacement control tension tests on the 3D-printed serpentine ribbons are performed with a strain rate of 0.1% s^{-1}. Engineering strains, i.e. total elongation divided by initial gauge length, are measured in the experiments. The intrinsic material strain-to-rupture ε_{cr} is measured using a straight specimen whereas the applied strains-to-rupture (or stretchability) ε_{app}^{cr} is measured for various serpentine ribbons. Although ABS is an elastic–plastic material and it ruptures within the plastic regime, the inner edge of the crest of the ABS serpentine is always subjected to pure tensile strain and small-scale yielding assumption has been validated for its failure (Pijnenburg et al., 2005), therefore the failure criterion $\varepsilon_{max}=\varepsilon_{cr}$ is still applicable. If experimentally measured $\varepsilon_{cr}/\varepsilon_{app}^{cr}$ can agree with analytical and FEM $\varepsilon_{max}/\varepsilon_{app}$, our models can be proved valid to capture the mechanics of plane strain serpentine ribbons. Analytical, FEM, and experimental results will be compared and discussed in Section 3.

3. Results

The strain distribution of three representative serpentine shapes are plotted in Fig. 2: A, $\alpha=0°$, w/R = 1/5, and l/R = 0, B, $\alpha=0°$, w/R = 1/5, and l/R = 1, and C, $\alpha=-20°$, w/R = 1/2, and l/R = 5. Analytical results are plotted just for the arcs and are always displayed in the left frames and unit cells modeled by FEM are displayed in the right frames. Contour plots obtained from the two distinct approaches look almost identical, suggesting the CB theory and FEM have validated each other. Attributing to symmetry and bending effect, maximum strains always occur at the center of the inner arc, as we have expected. As small deformation assumption is adopted in our theory and FEM, when subjected to an applied strain of 10%, the normalized maximum strain in a basic horseshoe serpentine is found to be 2% lower than that is calculated with nonlinear geometric relation turned on in ABAQUS. The amount of error increases as the applied strain increases. Among the three shapes plotted, the modified horseshoe in Fig. 2B gives the lowest normalized maximum strain ($\varepsilon_{max}/\varepsilon_{app}$ = 0.042), suggesting it is the most stretchable shape out of the three.

Effects of different geometric parameters are summarized in Figs. 3 and 4. Fig. 3 plots the effective stiffness of serpentine ribbons normalized by the stiffness of a straight ribbon as given in Eq. (7), which is equivalent to the ratio of reaction forces of serpentine (P) to straight ribbons (P') under the same applied displacements, P/P', as derived in Appendix B using energy methods. Closed-form analytical solution, Eq. (7), is plotted as curves and FEM results are plotted as dots. Unlike strain results to be discussed in Fig. 4, the FEM results match the analytical solutions all the way up to w/R = 1 in Fig. 3A, indicating that energy method can provide quite accurate global load–displacement results. When $\alpha=-90°$, the serpentine degrades to a straight bar, therefore P/P' = 1, as is obvious in Fig. 3C and D. According to Fig. 3A–D, the effects of all three variables on the effective stiffness are all monotonic: the smaller w/R, the bigger α, and the bigger l/R would all yield the lower effective stiffness. The results also indicate that the stiffness of a structure can be reduced by orders of magnitude by simply changing the structure configuration, which is the enabling mechanism of making tissue-like soft electronics out of serpentine-shaped stiff materials like silicon and gold (Kim et al., 2011, 2012). Because there are three independent geometric variables in Eq. (7), it can generate contour plots of the normalized effective stiffness as a function of two variables, l/R and α, with w/R fixed to be 1/5 (Fig. 3E) and 1/2 (Fig. 3F), respectively. The color scale represents the magnitude of the normalized stiffness and the blank zone represents inaccessible shapes due to the non-overlapping constraint which will be discussed in greater detail in Section 4. Red dots overlaid on the contour plot represent shapes with particular (α,l/R) combinations which has been simulated by FEM. Contour plots derive similar con-

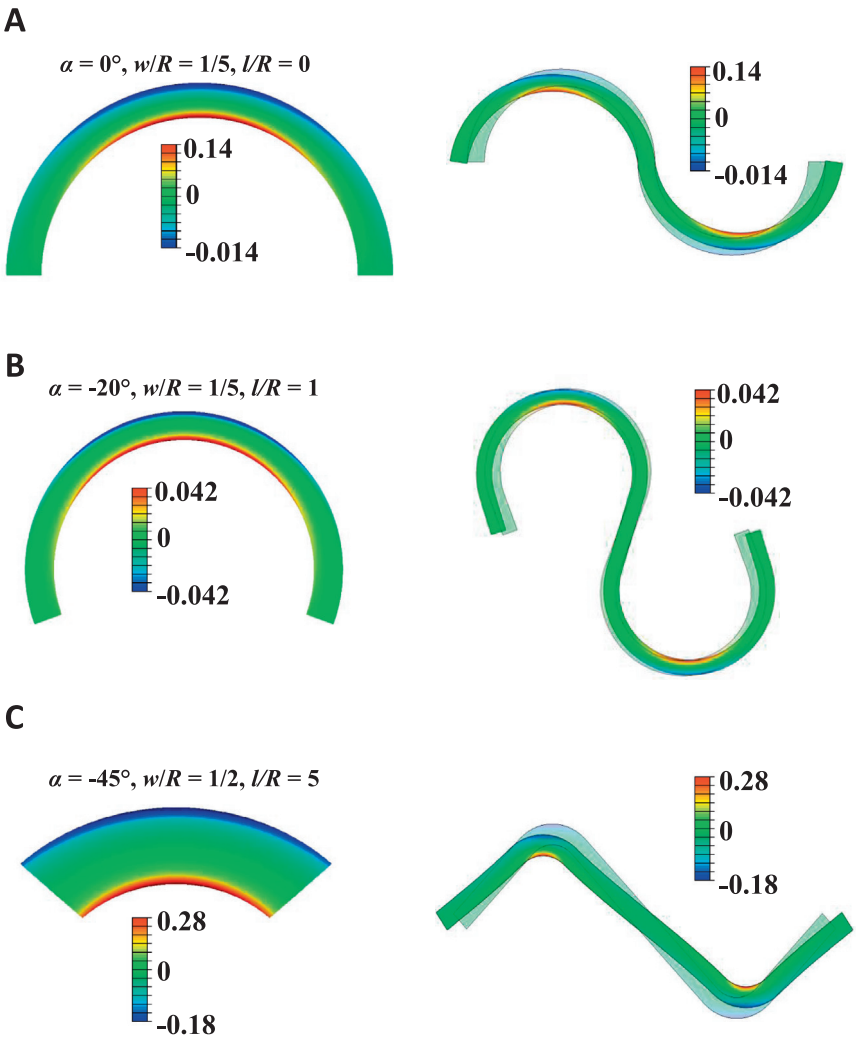

Fig. 2. Contour plots of strain fields obtained from CB theory (left frames) and FEM (right frames) with the geometric parameters fixed as (A) $\alpha = 0°$, $w/R = 1/5$, $l/R = 0$, (B) $\alpha = 20°$, $w/R = 1/5$, $l/R = 1$, and (C) $\alpha = -45°$, $w/R = 1/2$, $l/R = 5$.

clusions as the graphs but they offer more visualized illustrations and plot wider ranges of α and l/R.

Fig. 4 plots the normalized maximum strain as dots for FEM results and curves or contours for analytical results, as given in Eq. (8). Fig. 4A studies the effect of w/R at different l/R with α fixed to be 0°, which corresponds to Categories (a) and (b) in Fig. 1C. We found that FEM results match perfectly with the elasticity theory but not with the CB theory when the ratio w/R is bigger than 1/2, which is expected because CB theory made approximation on the strain energies for rectangular cross-sections to simplify the equations (Bickford, 1998). Fortunately, all of the commonly used serpentine shapes as depicted in Fig. 1C are within the limit of $w/R < 1/2$, so that the CB theory can accurately capture the maximum strain in these serpentines. As l/R gets larger, the CB theory can be accurate for larger range of w/R. The effects of w/R is monotonic, as w/R drops, $\varepsilon_{max}/\varepsilon_{app}$ can be reduced because the bending-induced strain can be reduced. In practice, w/R can hardly approach zero because the minimum width of the serpentine ribbons is limited by the resolution of the patterning technique (e.g. photolithography or laser cutting) and the requirement on electrical resistance of interconnects. For given w/R, $\varepsilon_{max}/\varepsilon_{app}$ is lower when the arm length l/R is longer when $\alpha = 0°$. For most of the cases plotted in Fig. 4A, $\varepsilon_{max}/\varepsilon_{app} < 1$, meaning the serpentine shape is helpful in reducing the intrinsic strains of the serpentine material, even when w approaches R. In practice, $w/R = 1/5$ is a popular scheme used in stretchable electronics (Kim et al., 2011; Yu et al., 2013). According to Fig. 4A, a strain reduction of more than ten folds can be achieved even without allowing out-of-plane buckling. Fig. 4B better illustrates the effect of l/R, with α fixed to be 0° and varying w/R, which corresponds to Category (c) in Fig. 1C. Long arms can help accommodate larger applied strain through rigid body rotation, hence larger l/R yields lower $\varepsilon_{max}/\varepsilon_{app}$, for all cases of w/R. The effect of α is given in Fig. 4C, with fixed $w/R = 1/5$ and varying l/R, which corresponds to Categories (d) and (e) in Fig. 1C. When $\alpha = -90°$, the serpentine ribbon degenerates into a straight ribbon, therefore $\varepsilon_{max}/\varepsilon_{app} = 1$ always holds. As α increases from $-90°$, $\varepsilon_{max}/\varepsilon_{app}$ first increases due to increased bending effect and then decreases due to enhanced rotational contribution. Note that $\varepsilon_{max}/\varepsilon_{app}$ may even exceed 1, indicating the maximum intrinsic strain in the material may exceed the applied strain due to superimposed tensile and bending strains. This surprising result alerts us that serpentine design is not always effective in reducing strain or in enhancing stretchability. Careful mechanics modeling should be performed to predict and evaluate the different serpentine shapes. As a comparison, we also fix $w/R = 1/2$ and showed the effects of α in Fig. 4D, which corresponds to Category (f) in Fig. 1C. The results are very similar to Fig. 4C except that there is a wider range of α where $\varepsilon_{max}/\varepsilon_{app}$ exceeds 1.

Similar to Fig. 3E and F, contour plots of $\varepsilon_{max}/\varepsilon_{app}$ as a function of α and l/R for two different w/R are offered in Fig. 4E and F using

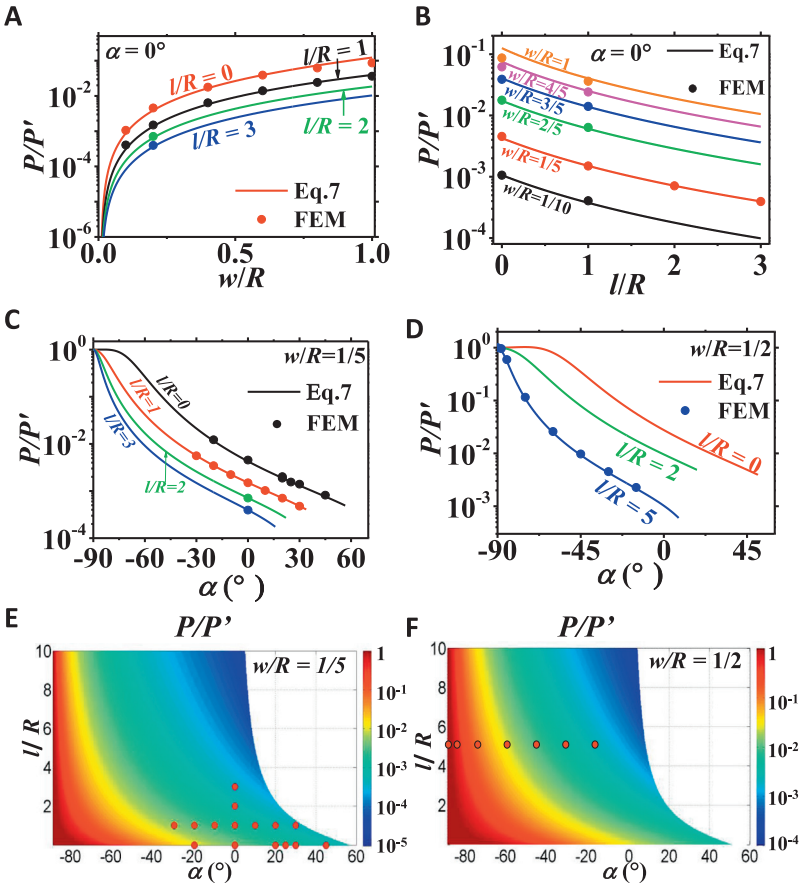

Fig. 3. (A) Plot of normalized stiffness as a function of w/R when $\alpha = 0°$ and l/R is varying. (B) Plot of normalized stiffness as a function of l/R when $\alpha = 0°$ and w/R is varying. (C) Plot of normalized stiffness as a function of α when $w/R = 1/5$ and l/R is varying. (D) Plot of normalized stiffness as a function of α when $w/R = 1/2$ and l/R is varying. (E) Contour plot of normalized stiffness as a function of α and l/R when $w/R = 1/5$. The red dots represent the cases that have been modeled by FEM. The blank region represents the inaccessible shapes due to the non-overlapping constraint. (F) Contour plot of normalized stiffness as a function of α and l/R when $w/R = 1/2$. (For interpretation of the references to colour in this figure legend, the reader is referred to the web version of this article.)

Eq. (8). The color scale represents the magnitude of the normalized maximum strain and the blank zone represents inaccessible shapes. For example, when α is large, there is an upper limit of the arm length because otherwise the ribbons will overlap. When α asymptotically approaches 0° along the edge of the contour, horseshoe degenerates into a U-shape and therefore, l/R could approach infinite if no other geometric constraints are considered. We will provide more detailed discussions on geometric constraints in Section 4. Red dots are used to denote cases where FEM results are available. Unlike on stiffness, the effect of α on strain is clearly not monotonic unless l/R is very large, i.e. the arm is very long. As α increases from the far negative regime, $\varepsilon_{max}/\varepsilon_{app}$ will first increase to a peak value before it starts to decrease. When α falls somewhere between −90° and −45°, $\varepsilon_{max}/\varepsilon_{app}$ may even exceed 1, meaning these serpentine shapes are even less stretchable compared to their straight counterparts. According to the contour plots, the effect of l/R is monotonic under most values of α but not all. Both Fig. 4E and F show that when α falls in the far negative regime, the maximum strain will first increase with increased l/R due to increased bending moment and then decrease because of the decreased structure stiffness.

The plots in Fig. 4 has limited l/R to 10 but when $\alpha = 0°$, l/R can be unlimited. The normalized maximum strain when $\alpha = 0°$ can be simplified from Eq. (8) to be a function of just w/R and l/R:

$$\frac{\varepsilon_{max}}{\varepsilon_{app}} = \frac{\frac{w}{R}\left[\frac{12}{2-\frac{w}{R}} + \left(\frac{12}{2-\frac{w}{R}} - \frac{w}{R}\right)\frac{l}{2R}\right]}{\frac{l^3}{2R^3} + \frac{3\pi l^2}{2R^2} + 12\frac{l}{R} + 3\pi + \frac{w^2}{R}\left[\frac{\pi}{8}\frac{l^2}{R^2} + \frac{3}{4}\frac{l}{R}\frac{E}{G}\right]} \tag{9}$$

To study the effect of long-armed serpentines as shown in Fig. 5A, Fig. 5B plots $\varepsilon_{max}/\varepsilon_{app}$ in log scale as a function of l/R up to 100 using Eq. (9). It is found that increasing l/R is a very effective way to reduce the max intrinsic strains in serpentines, which will lead to significant enhancement of the stretchability, up to three orders of magnitude, even without any out-of-plane buckling or twisting. This means that a brittle material with an intrinsic strain-to-rupture of 1% can be made to deploy by 1000% when they are patterned into long-armed serpentines like Fig. 5A. This formulation also explains why the gold serpentine network can be as expandable as spider webs (up to 1600%) (Lanzara et al., 2010).

Comparison between modeling and experimental results is offered in Fig. 6. Fig. 6A shows three different sets of 3D printed serpentine specimens with systematically changing shapes. Every specimen shown in this figure has a thickness of 0.1 in and a ribbon width of 0.039 in. Because of the relatively large thickness, the serpentine specimens undergo in-plane elongation during the tensile tests, which is compatible with our plane strain assumption for the models. As mentioned in Section 2, measured $\varepsilon_{cr}/\varepsilon_{app}^{cr}$ are compared with CB theory and FEM results as given by Fig. 6B–D. Fig. 6B plots $\varepsilon_{max}/\varepsilon_{app}$ as a function of l/R with fixed $\alpha = 0°$ and $w/R = 1/5$. Fig. 6C and D plot $\varepsilon_{max}/\varepsilon_{app}$ as a function of α, with $w/R = 1/5$, $l/R = 0$ (Fig. 6C) and $w/R = 1/2$, $l/R = 5$ (Fig. 6D), respectively.

In summary, we have obtained consistent results for the maximum strain and stiffness of freestanding serpentines under linear elastic, plane strain assumptions using CB theories, FEM, and experimental approaches. Effects of α, w/R, and l/R are carefully

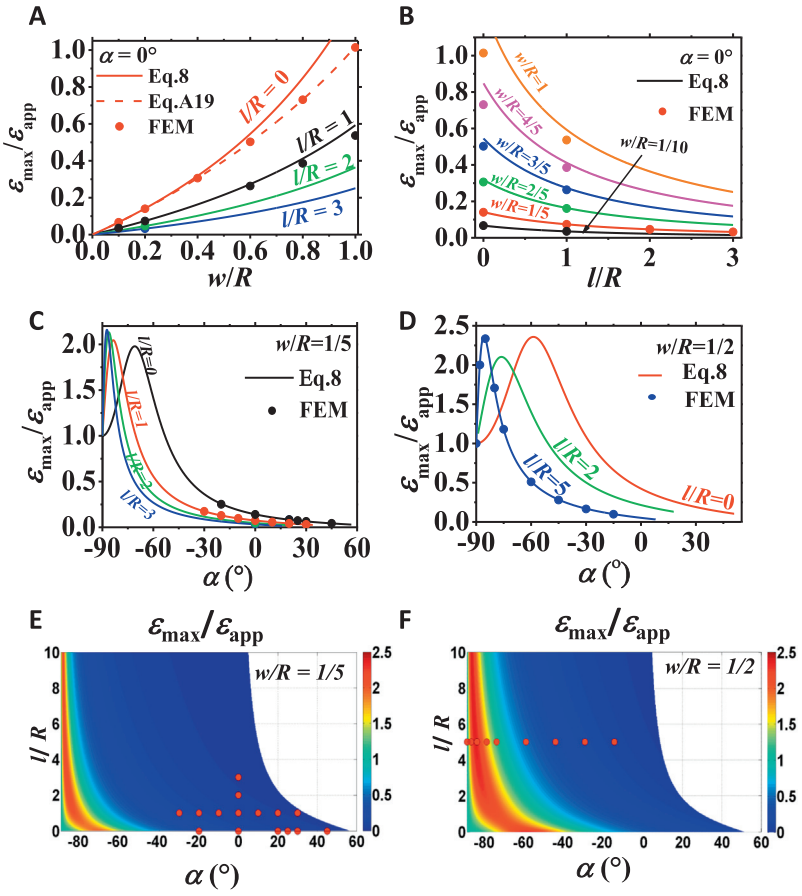

Fig. 4. (A) Plot of $\varepsilon_{max}/\varepsilon_{app}$ as a function of w/R when $\alpha = 0°$ and l/R is varying. (B) Plot of $\varepsilon_{max}/\varepsilon_{app}$ as a function of l/R when $\alpha = 0°$ and w/R is varying. (C) Plot of $\varepsilon_{max}/\varepsilon_{app}$ as a function of α when $w/R = 1/5$ and l/R is varying. (D) Plot of $\varepsilon_{max}/\varepsilon_{app}$ as a function of α when $w/R = 1/2$ and l/R is varying. (E) Contour plot of $\varepsilon_{max}/\varepsilon_{app}$ as a function of α and l/R when $w/R = 1/5$. The red dots represent the cases that have been modeled by FEM. The blank region represents the inaccessible shapes due to the non-overlapping constraint. (F) Contour plot of $\varepsilon_{max}/\varepsilon_{app}$ as a function of α and l/R when $w/R = 1/2$. (For interpretation of the references to colour in this figure legend, the reader is referred to the web version of this article.)

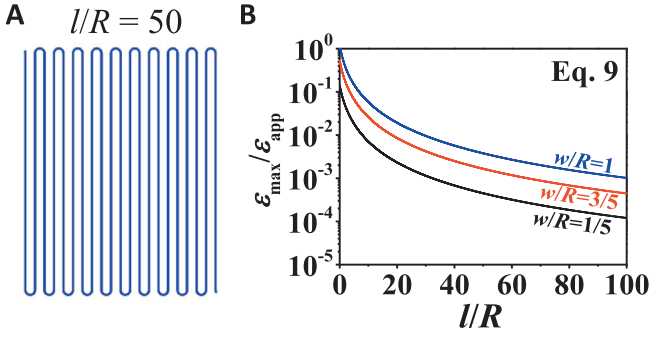

Fig. 5. (A) Illustration of ultra-long-armed serpentine. (B) Eq. (9) is plotted for ultra large l/R: normalized maximum strain can be reduced by orders of magnitude as arm length is orders larger than the arc radius.

revealed. In general, the narrower ribbon, the larger arc radius and arc angle, and the longer arm length will yield lower effective stiffness and intrinsic strain. However, although serpentines are always effective in reducing structure stiffness, not all serpentines can lead to strain reduction. A few unexpected behaviors are found at arc angles that are close to straight bars. Orders of magnitude enhancement of stretchability can be achieved when $\alpha = 0°$ and l/R approaches infinite.

4. Optimal serpentine shape under practical constraints

In practical circuit design, stretchable serpentine interconnects are usually subjected to design and fabrication constraints. For example, although we find in Section 3 that narrower serpentines are always more compliant and more stretchable, the width of serpentines cannot approach zero due to limitations of fabrication resolution as well as electrical resistance considerations. Assume that a practically possible minimum width is pre-determined, this section will demonstrate how to construct the most stretchable serpentine shape under certain geometric constraints.

For a given w, the mathematical procedure of finding out the optimal shape under certain geometric constraint is to identify three equations to solve for three unknowns, α, w/R, and l/R. The first equation comes from the non-overlapping requirement, i.e. the distance between the two nearest ribbons, X as defined in Fig. 7A, should be larger or equal to 0, i.e.

$$X = \left(R - \frac{w}{2}\right)\cos\alpha - l\sin\alpha - \left(R + \frac{w}{2}\right)(1 - \cos\alpha) = 0 \tag{10}$$

Solving this equation we can get the largest possible α for given $(w/R, l/R)$ combinations:

$$\alpha_{max} = 2 \cdot \arctan\left(\frac{-2\frac{l}{R}}{6 + \frac{w}{R}} + \sqrt{\frac{2\left(2\frac{l^2}{R} + \frac{w}{R} + 6\right)}{\left(6 + \frac{w}{R}\right)^2} - 1}\right) \tag{11}$$

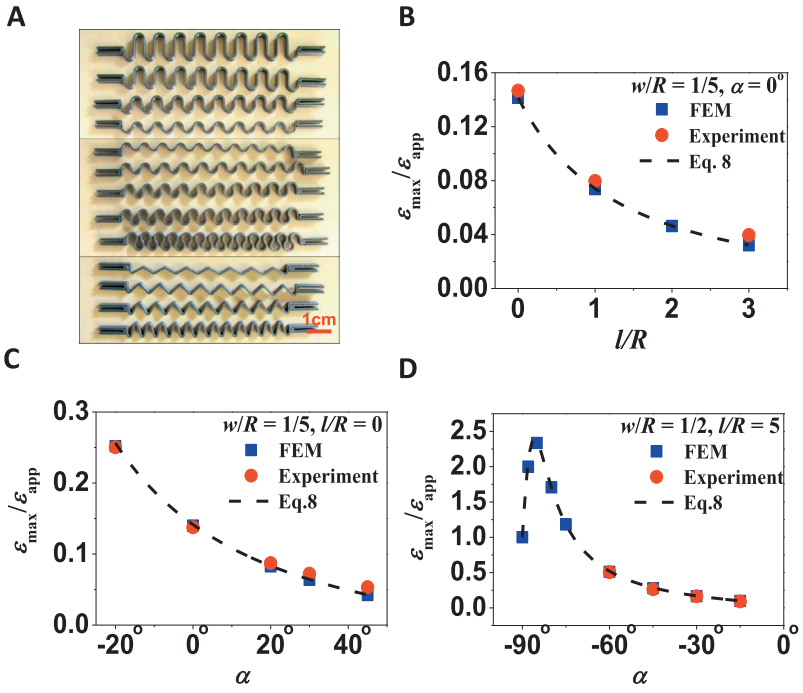

Fig. 6. (A) 3D-printed thick serpentine ribbons to be tested by uniaxial tension. Intrinsic strain-to-rupture of the material, ε_{cr}, is measured using straight specimens. Stretchability, ε_{app}^{cr}, is measured as the applied strain-to-rupture of serpentine specimens. Therefore, experimental $\varepsilon_{cr}/\varepsilon_{app}^{cr}$ should be equivalent to $\varepsilon_{max}/\varepsilon_{app}$ in theory and FEM. (B) Comparison of results from CB theory (dashed curve), FEM (blue markers), and experiments (red markers) for various l/R. (C) and (D), comparison of results from CB theory (dashed curve), FEM (blue markers), and experiments (red markers) for various α at different w/R. (For interpretation of the references to colour in this figure legend, the reader is referred to the web version of this article.)

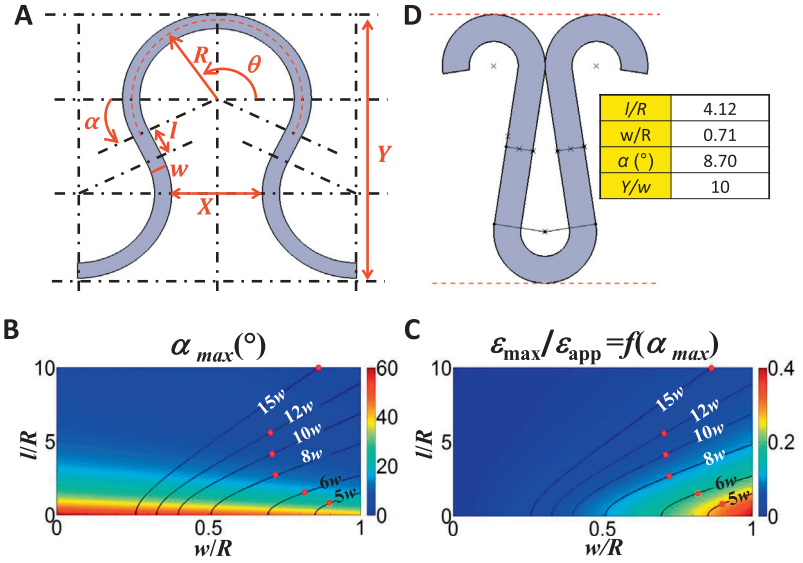

Fig. 7. (A) Illustration of geometric constraints. For example, non-overlapping constraint: $X = 0$ and finite breadth constraints: Y is bonded. (B) Contour plot of the largest possible values of α, α_{max}, as a function of w/R and l/R considering the non-overlapping constraint given by Eq. (10). (C) Contour plot of $\varepsilon_{max}/\varepsilon_{app}$ values as a function of w/R, l/R and α_{max}, as given by Eq. (8). Optimal shape can be determined by the position of minimum $\varepsilon_{max}/\varepsilon_{app}$ values on each isoline representing a constant Y. (D) Optimal serpentine shape under the constraint of $X = 0$ and $Y = 10w$.

The second equation reflects the finite breadth constraint when considering limited real estate on the circuit board, e.g. $Y = 10w$, where the breadth Y is defined in Fig. 7A:

$$Y = 2R + w + 2R\sin\alpha + l\cos\alpha = 10w \tag{12}$$

The third equation is the minimization of $\varepsilon_{max}/\varepsilon_{app}$, i.e. minimizing the values given by Eq. (8). Since the optimization problem now reduces to a problem of minimization under two constraints, we can certainly use Lagrangian multiplier. Since the final results are too complicated to show, solutions to the three variables can be more easily illustrated with two contour plots. Fig. 7B plots the value of α_{max} as a function of w/R and l/R, as derived in Eq. (11). Plugging that into Eq. (8) will yield the value of $\varepsilon_{max}/\varepsilon_{app}$ as a function of w/R and l/R as plotted in Fig. 7C. The finite breadth constraint given in Eq. (12) can be plotted as a curve in the $(w/R, l/R)$ space, and the point on the curve which yields the lowest value of $\varepsilon_{max}/\varepsilon_{app}$ represents the most stretchable shape, which is highlighted by a red dot in Fig. 7C. Plot the coordinates $(w/R, l/R)$

of this dot read from Fig. 7C in Fig. 7B, the corresponding α_{max} value can be read from the color scale and hence all three parameters α, w/R, and l/R are uniquely determined. Their dimensionless nature dictates that the actual dimension of the optimal serpentine is completely scalable with the ribbon width, w. In addition to $10w$, Fig. 7B and C also plots isolines of various breadth values, from $5w$ to $15w$. For finite breadth of $10w$, the optimal serpentine design can be finally determined by reading the figures as $\alpha = 8.7°$, $w/R = 0.71$, and $l/R = 4.12$. Therefore, with given constraints of w and Y, the most stretchable serpentine shape is depicted in Fig. 7D. Shape optimization under other geometric constraints can be formulated following similar approaches.

5. Conclusions

We have applied plane strain CB theories and FEM to study the effects of several dimensionless geometric parameters on the normalized effective stiffness and maximum strain (or stretchability) of freestanding serpentine ribbons in a systematic manner. The CB theories are able to accurately predict $\varepsilon_{max}/\varepsilon_{app}$ when w/R is small or l/R is large, which is validated by both FEM and tension tests of 3D-printed serpentine specimens. Our study reveals that ribbons with small w/R, large l/R and large α are going to be compliant and stretchable with some rare exceptions. The stretchability can be enhanced by several orders when l/R approaches infinite. In practical stretchable circuit designs, there are often design and fabrication constraints such as non-overlapping requirement or finite breadth constraint. In these cases, the optimal serpentine shapes can be analytically determined using our closed-form CB solutions.

Acknowledgements

This work is supported by the NSF CMMI award under Grant No. 1301335 and the NASCENT (Nanomanufacturing Systems for Mobile Computing and Mobile Energy Technologies) Center under NSF Grant No. 1160494. T.W. acknowledges the fellowship from the Ministère Français de l'Enseignement Supérieur et de la Recherche, the Arts et Métiers Paristech. N.L. acknowledges the enlightening discussions with Prof. K. Ravi-Chandar.

Appendix A. Elasticity theory

In elasticity theory, the elastic field of equations are given by:

i. The strain–displacement relation (tensor notation):

$$\varepsilon_{ij} = \frac{1}{2}(u_{i,j} + u_{j,i}) \tag{A1}$$

where ε_{ij} is the strain tensor and u_i is the displacement.

ii. The equilibrium equations:

$$\sigma_{ij,i} + F_j = 0 \tag{A2}$$

where $\sigma_{ij,i}$ is the stress tensor and F_j is the body forces.

iii. Hooke's law:

$$\sigma_{ij} = \lambda\varepsilon_{kk}\delta_{ij} + 2\mu\varepsilon_{ij} \tag{A3}$$

where λ is Lamé's constant, δ_{ij} is Kronecker's delta and μ the shear modulus.

iv. Saint Venant compatibility equations:

$$\varepsilon_{ij,kl} + \varepsilon_{kl,ij} - \varepsilon_{ik,jl} - \varepsilon_{jl,ik} = 0 \tag{A4}$$

In our case, we are dealing with a plane stain problem as depicted in Fig. 1B.

The deformation field in plane strain can be reduced to: $u_x = u_x(x,y)$, $u_y = u_y(x,y)$ and $u_z = 0$.

By Eq. (A1), the strains become in plane:

$$\varepsilon_x = \frac{\partial u_x}{\partial x}, \quad \varepsilon_y = \frac{\partial u_y}{\partial y}, \quad \varepsilon_{xy} = \frac{1}{2}\left(\frac{\partial u_y}{\partial x} + \frac{\partial u_x}{\partial y}\right)$$

$$\varepsilon_z = \varepsilon_{xz} = \varepsilon_{yz} = 0 \tag{A5}$$

The isotropic form of Hook's Law gives:

$$\sigma_x = \lambda\left(\frac{\partial u_x}{\partial x} + \frac{\partial u_y}{\partial y}\right) + 2\mu\frac{\partial u_x}{\partial x}$$

$$\sigma_y = \lambda\left(\frac{\partial u_x}{\partial x} + \frac{\partial u_y}{\partial y}\right) + 2\mu\frac{\partial u_y}{\partial y}$$

$$\sigma_z = \upsilon(\sigma_x + \sigma_y)$$

$$\tau_{xy} = \mu\left(\frac{\partial u_y}{\partial x} + \frac{\partial u_x}{\partial y}\right)$$

$$\tau_{xz} = \tau_{yz} = 0 \tag{A6}$$

The equilibrium equations give:

$$\frac{\partial \sigma_x}{\partial x} + \frac{\partial \tau_{xy}}{\partial y} + F_x = 0$$

$$\frac{\partial \sigma_y}{\partial y} + \frac{\partial \tau_{xy}}{\partial x} + F_y = 0 \tag{A7}$$

Finally the Saint Venant's equations become:

$$\frac{\partial^2 \varepsilon_x}{\partial y} + \frac{\partial^2 \varepsilon_y}{\partial x} = 2\frac{\partial^2 \varepsilon_{xy}}{\partial x \partial y} \tag{A8}$$

Combining Eqs. (A5) and (A8) and vanishing the body forces, the problem is reduced to the following form:

$$\nabla^4 \phi = 0 \tag{A9}$$

where ϕ is the Airy stress function.

In our case, curved beam with end loads, the Airy stress function takes the form:

$$\phi(r,\theta) = R(r)\cos n\theta \tag{A10}$$

Plugging into Eq. (A9) yields the following solution,

$$\phi = \left(Ar^3 + \frac{B}{r} + Cr + Dr\log r\right)\sin\theta \tag{A11}$$

In elasticity, we have the following relations in polar coordinate:

$$\sigma_r = \frac{1}{r}\frac{\partial \phi}{\partial r} + \frac{1}{r^2}\frac{\partial^2 \phi}{\partial \theta^2}$$

$$\sigma_\theta = \frac{\partial^2 \phi}{\partial r^2} \tag{A12}$$

$$\tau_{r\theta} = -\frac{\partial}{\partial r}\left(\frac{1}{r}\frac{\partial \phi}{\partial \theta}\right)$$

In our case, this theory is applied to a specific serpentine shape where $l/R = 0$ and $\alpha = 0°$.

As a consequence,

$$\sigma_r = 2A\left(r + \frac{a^2b^2}{r^3} - \frac{a^2+b^2}{r}\right)\sin\theta$$

$$\sigma_\theta = 2A\left(3r - \frac{a^2b^2}{r^3} - \frac{a^2+b^2}{r}\right)\sin\theta \tag{A13}$$

$$\tau_{r\theta} = -2A\left(r + \frac{a^2b^2}{r^3} - \frac{a^2+b^2}{r}\right)\cos\theta$$

where

$$a = R - \frac{w}{2} \text{ and } b = R + \frac{w}{2}$$

$$2A = \frac{-P}{a^2 - b^2 + (a^2 + b^2)\ln\frac{b}{a}} \tag{A14}$$

Applying the strain–displacement relation, the reaction force is obtained as

$$P = \bar{E}\frac{u_0}{2}\frac{a^2 - b^2 + (a^2 + b^2)\ln\frac{b}{a}}{\pi(a^2 + b^2)} = \bar{E}\frac{u_0}{2\pi}\left(-\frac{4\frac{w}{R}}{4 + \frac{w^2}{R^2}} + \ln\left(-1 - \frac{4}{-2 + \frac{w}{R}}\right)\right) \tag{A15}$$

The maximal strain ε_{max} is obtained for $\theta = \frac{\pi}{2}$ and $r = a$, so that by Hook's law:

$$\varepsilon_{max} = \varepsilon_\theta\left(\theta = \frac{\pi}{2}; r = a\right) = \frac{\sigma_\theta\left(\theta = \frac{\pi}{2}; r = a\right)}{\bar{E}} \tag{A16}$$

Thus

$$\varepsilon_{max} = -u_0\frac{(a^2 - b^2) + (a^4 - b^4)\ln\frac{b}{a}}{\pi a(a^2 + b^2)} \tag{A17}$$

According to Fig. 1A, the applied strain is given by $2u_0/S$:

$$\varepsilon_{app} = \frac{u_0}{2(R\cos\alpha - l\sin\alpha)} \tag{A18}$$

Lastly, we can obtain the normalized strain

$$\frac{\varepsilon_{max}}{\varepsilon_{app}} = -\frac{(a^2 - b^2) + (a^4 - b^4)\ln\frac{b}{a}}{\frac{\pi}{2}a(a^2 + b^2)}\left(R\cos\alpha - \frac{l}{2}\sin\alpha\right) \tag{A19}$$

This exact elasticity solution is plotted as the dashed curve in Fig. 4A, which matches with FEM perfectly.

Appendix B. Curved beam theory

The force equilibrium of a curved beam as shown in Fig. 1B yields:

$$N_{arc} = P\cos\theta \tag{A20}$$

$$V_{arc} = -P\sin\theta \tag{A21}$$

$$M_{arc} = PR(\sin\alpha + \cos\theta) + P\frac{l}{2}\cos\alpha \tag{A22}$$

$$M_{arm} = Ps\cos\alpha \tag{A23}$$

$$V_{arm} = -P\cos\alpha \tag{A24}$$

$$N_{arm} = P\sin\alpha \tag{A25}$$

where N is the internal normal traction at the centroid of the cross-section, M is the internal moment.

The energy method (Castigliano) provides us the link between the applied displacement u_0 and the reaction force P:

$$\frac{u_0}{2} = \frac{\partial U}{\partial P} = \frac{\partial(U_{arm} + U_{arc})}{\partial P} \tag{A26}$$

where U is the elastic energy:

$$U_{arm} = \int_0^{\frac{l}{2}}\left[\kappa\frac{V_{arm}{}^2}{2GA} + \frac{N_{arm}{}^2}{2\bar{E}A} + \frac{M_{arm}{}^2}{2\bar{E}I_2}\right]ds \tag{A27}$$

and

$$U_{arc} = \int_0^{\alpha+\frac{\pi}{2}}\left[\frac{(N_{arc}R - M_{arc})^2}{2\bar{E}AR} + \frac{M_{arc}{}^2}{2\bar{E}I_2}\right]Rd\theta \tag{A28}$$

where $\kappa = 1.5$, is the correction coefficient for strain energy in a rectangular section.

This yields

$$\frac{\partial U_{arc}}{\partial P} = P\left[\frac{R}{2\bar{E}}\left[\frac{(\pi + 2\alpha)\left(\frac{l}{2}\cos\alpha + R\sin\alpha\right)^2}{AR} + \frac{8R\cos\alpha\left(\frac{l}{2}\cos\alpha + R\sin\alpha\right) - R\sin 2\alpha}{2I_2} + \frac{(\pi + 2\alpha)\left(\frac{l}{4} + 2R + \left(\frac{l}{2} - R\right)\left(\frac{l}{2} + R\right)\cos 2\alpha + 2\frac{l}{2}R\sin 2\alpha\right)}{2I_2}\right]\right] \tag{A29}$$

and

$$\frac{\partial U_{arm}}{\partial P} = P\frac{l}{2}\left(\frac{3\cos^2\alpha}{2AG} + \frac{\frac{l^2}{4}\cos^2\alpha}{3I_2\bar{E}} + \frac{\sin^2\alpha}{A\bar{E}}\right) \tag{A30}$$

For plane strain, we assume thickness $h = 1$ so that

$$A = w, \quad I_2 = \frac{w^3}{12}, \text{ and } \bar{E} = \frac{E}{1 - v} \tag{A31}$$

Thereby we obtain

$$\frac{u_0}{2} = \frac{PR^3}{w^3\bar{E}}\begin{bmatrix}\cos^2\alpha\left(\frac{l^3}{2R^3} + 3\left(\frac{\pi}{2} + \alpha\right)\frac{l^2}{R^2} + 12\frac{l}{R} - 12\left(\frac{\pi}{2} + \alpha\right)\right) \\ + \sin 2\alpha\left(6\left(\frac{\pi}{2} + \alpha\right)\frac{l}{R} + 9\right) \\ + \frac{w^2}{R}\left[\left(\frac{\pi}{2} + \alpha\right)\left(\frac{l}{2R}\cos\alpha + \sin\alpha\right)^2 + \frac{l}{2R}\left(\sin\alpha + \frac{3\bar{E}}{2G}\cos^2\alpha\right)\right] + 18\left(\frac{\pi}{2} + \alpha\right)\end{bmatrix} \tag{A32}$$

Since the stiffness of a straight ribbon is given by $\bar{E}w/S$, where S is given in Eq. (1), the normalized effective stiffness can be expressed as:

$$\frac{PS}{2\bar{E}wu_0} = \frac{\frac{w}{R}\left(\cos\alpha - \frac{l}{2R}\sin\alpha\right)}{2\begin{bmatrix}\cos^2\alpha\left(\frac{l^3}{2R^3} + 3\left(\frac{\pi}{2} + \alpha\right)\frac{l^2}{R^2} + 12\frac{l}{R} - 12\left(\frac{\pi}{2} + \alpha\right)\right) \\ + \sin 2\alpha\left(6\left(\frac{\pi}{2} + \alpha\right)\frac{l}{R} + 9\right) \\ + \frac{w^2}{R}\left[\left(\frac{\pi}{2} + \alpha\right)\left(\frac{l}{2R}\cos\alpha + \sin\alpha\right)^2 + \frac{l}{2R}\left(\sin^2\alpha + \frac{3\bar{E}}{2G}\cos^2\alpha\right)\right] + 18\left(\frac{\pi}{2} + \alpha\right)\end{bmatrix}} \tag{A33}$$

which is the same as Eq. (7).

According to Fig. 1A, the applied strain is given by $2u_0/S$:

$$\varepsilon_{app} = \frac{u_0}{2\left(R\cos\alpha - \frac{l}{2}\sin\alpha\right)} \tag{A34}$$

The hoop stress in the arc is given by:

$$\sigma_{\theta\theta} = \frac{N - \frac{M}{R}}{A} - \frac{My}{\left(1+\frac{y}{R}\right)I_2} \tag{A35}$$

where A is the cross-sectional area and y is the distance from the centerline.

And

$$I_2 = \int \frac{Ry^2}{R+y}dA \tag{A36}$$

Applying Hook's law, the hoop strain is easily obtained by:

$$\varepsilon_{\theta\theta} = \frac{\sigma_{\theta\theta}}{\bar{E}}$$

As maximum strain occurred at the center of the curvature, for $\theta = 0^\circ$ and $y = -w/2$, and by the equilibrium equations the maximum strain obtained by the curved beam theory is given by:

$$\varepsilon_{max} = \frac{P\left(-\sin\alpha + \frac{l}{2R}\cos\alpha\right)}{\bar{E}w} + \frac{6P\left(R(\sin\alpha+1) + \frac{l}{2}\cos\alpha\right)}{\left(1-\frac{w}{2R}\right)\bar{E}w^2} \tag{A37}$$

Combining Eqs. (A34) and (A37), the normalized maximum strain is

$$\frac{\varepsilon_{max}}{\varepsilon_{app}} = \frac{\frac{w}{R}\left[\frac{12}{2-\frac{w}{R}} + \left(\frac{12}{2-\frac{w}{R}} - \frac{w}{R}\right)(\sin\alpha + \frac{l}{2R}\cos\alpha)\right](\cos\alpha - \frac{l}{2R}\sin\alpha)}{\left[\begin{array}{c}\cos^2\alpha\left(\frac{l^3}{2R^3} + 3\left(\frac{\pi}{2}+\alpha\right)\frac{l^2}{R^2} + 12\frac{l}{R} - 12\left(\frac{\pi}{2}+\alpha\right)\right) \\ +\sin 2\alpha\left(6\left(\frac{\pi}{2}+\alpha\right)\frac{l}{R}+9\right) \\ +\frac{w^2}{R}\left[\left(\frac{\pi}{2}+\alpha\right)\left(\frac{l}{2R}\cos\alpha + \sin\alpha\right)^2 + \frac{l}{2R}\left(\sin^2\alpha + \frac{3\bar{E}}{2G}\cos^2\alpha\right)\right] + 18\left(\frac{\pi}{2}+\alpha\right)\end{array}\right]} \tag{A38}$$

which is the same as Eq. (8).

For special cases:

$$\begin{array}{ll} & \frac{\varepsilon_{max}}{\varepsilon_{app}} \\ l = 0 & \frac{\frac{w}{R}\left[\frac{12}{2-\frac{w}{R}} + \left(\frac{12}{2-\frac{w}{R}} - \frac{w}{R}\right)\sin\alpha\right]\cos\alpha}{-12\left(\frac{\pi}{2}+\alpha\right)\cos^2\alpha + 9\sin 2\alpha + \frac{w^2}{R}\left(\frac{\pi}{2}+\alpha\right)\sin^2\alpha + 18\left(\frac{\pi}{2}+\alpha\right)} \\ \alpha = 0^\circ & \frac{\frac{w}{R}\left[\frac{12}{2-\frac{w}{R}} + \left(\frac{12}{2-\frac{w}{R}} - \frac{w}{R}\right)\frac{l}{2R}\right]}{\frac{l^3}{2R^3} + \frac{3\pi l^2}{2R^2} + 12\frac{l}{R} + 3\pi + \frac{w^2}{R^2}\left[\frac{\pi}{8}\frac{l^2}{R^2} + \frac{3}{4}\frac{l}{R}\frac{\bar{E}}{G}\right]} \\ l = 0 & \text{and } \alpha = 0^\circ \\ & \frac{1}{3\pi}\frac{w}{R}\frac{12}{2-\frac{w}{R}} \end{array}$$

References

Beyar, R., Roguin, A., Hamburger, J., Saaiman, A., Bartorelli, A.L., DiMario, C., Colombo, A., Hamm, C.W., White, C.J., Marco, J., Serruys, P.W., 1997. Multicenter pilot study of a serpentine balloon-expandable stent (beStent(TM)): acute angiographic and clinical results. J. Interventional Cardiol. 10 (4), 277–286.

Bickford, W.B., 1998. Advanced Mechanics of Materials. Addison-Wesley, Menlo Park, CA.

Brosteaux, D., Axisa, F., Gonzalez, M., Vanfleteren, J., 2007. Design and fabrication of elastic interconnections for stretchable electronic circuits. IEEE Electron Device Lett. 28 (7), 552–554.

Gleskova, H., Wagner, S., Suo, Z., 1999. Failure resistance of amorphous silicon transistors under extreme in-plane strain. Appl. Phys. Lett. 75 (19), 3011–3013.

Gray, D.S., Tien, J., Chen, C.S., 2004. High-conductivity elastomeric electronics. Adv. Mater. 16 (5), 393.

Hommel, M., Kraft, O., 2001. Deformation behavior of thin copper films on deformable substrates. Acta Mater. 49 (19), 3935–3947.

Hsu, Y.Y., Gonzalez, M., Bossuyt, F., Axisa, F., Vanfleteren, J., De Wolf, I., 2009. In situ observations on deformation behavior and stretching-induced failure of fine pitch stretchable interconnect. J. Mater. Res. 24 (12), 3573–3582.

Huang, X., Yeo, W.H., Liu, Y.H., Rogers, J.A., 2012. Epidermal differential impedance sensor for conformal skin hydration monitoring. Biointerphases 7 (52), 1–9.

Kang, Y.J., Yoo, C.H., 1994. Thin-walled curved beams Formulation of nonlinear equations. J. Eng. Mech. ASCE 120 (10), 2072–2101.

Khang, D., Jiang, H., Huang, Y., Rogers, J., 2006. A stretchable form of single-crystal silicon for high-performance electronics on rubber substrates. Science 311 (5758), 208–212.

Kim, D.H., Song, J.Z., Choi, W.M., Kim, H.S., Kim, R.H., Liu, Z.J., Huang, Y.Y., Hwang, K.C., Zhang, Y.W., Rogers, J.A., 2008. Materials and noncoplanar mesh designs for integrated circuits with linear elastic responses to extreme mechanical deformations. Proc. Nat. Acad. Sci. USA 105 (48), 18675–18680.

Kim, R.H., Bae, M.H., Kim, D.G., Cheng, H.Y., Kim, B.H., Kim, D.H., Li, M., Wu, J., Du, F., Kim, H.S., Kim, S., Estrada, D., Hong, S.W., Huang, Y.G., Pop, E., Rogers, J.A., 2011. Stretchable, transparent graphene interconnects for arrays of microscale inorganic light emitting diodes on rubber substrates. Nano Lett. 11 (9), 3881–3886.

Kim, D.H., Lu, N.S., Ma, R., Kim, Y.S., Kim, R.H., Wang, S.D., Wu, J., Won, S.M., Tao, H., Islam, A., Yu, K.J., Kim, T.I., Chowdhury, R., Ying, M., Xu, L.Z., Li, M., Chung, H.J., Keum, H., McCormick, M., Liu, P., Zhang, Y.W., Omenetto, F.G., Huang, Y.G., Coleman, T., Rogers, J.A., 2011. Epidermal electronics. Science 333 (6044), 838–843.

Kim, D.H., Lu, N.S., Ghaffari, R., Kim, Y.S., Lee, S.P., Xu, L.Z., Wu, J.A., Kim, R.H., Song, J.Z., Liu, Z.J., Viventi, J., de Graff, B., Elolampi, B., Mansour, M., Slepian, M.J., Hwang, S., Moss, J.D., Won, S.M., Huang, Y.G., Litt, B., Rogers, J.A., 2011. Materials for multifunctional balloon catheters with capabilities in cardiac electrophysiological mapping and ablation therapy. Nat. Mater. 10 (4), 316–323.

Kim, D.H., Ghaffari, R., Lu, N.S., Wang, S.D., Lee, S.P., Keum, H., D'Angelo, R., Klinker, L., Su, Y.W., Lu, C.F., Kim, Y.S., Ameen, A., Li, Y.H., Zhang, Y.H., de Graff, B., Hsu, Y.Y., Liu, Z.J., Ruskin, J., Xu, L.Z., Lu, C., Omenetto, F.G., Huang, Y.G., Mansour, M., Slepian, M.J., Rogers, J.A., 2012. Electronic sensor and actuator webs for large-area complex geometry cardiac mapping and therapy. Proc. Nat. Acad. Sci. USA 109 (49), 19910–19915.

Kim, D.H., Ghaffari, R., Lu, N.S., Rogers, J.A., 2012a. Flexible and stretchable electronics for bio-integrated devices. Annu. Rev. Biomed. Eng. 14, 113–128.

Kim, D.H., Lu, N.S., Ghaffari, R., Rogers, J.A., 2012b. Inorganic semiconductor nanomaterials for flexible and stretchable bio-integrated electronics. NPG Asia Mater. 4, e15.

Kim, D.H., Lu, N.S., Huang, Y.G., Rogers, J.A., 2012c. Materials for stretchable electronics in bioinspired and biointegrated devices. MRS Bull. 37 (3), 226–235.

Lacour, S.P., Jones, J., Wagner, S., Li, T., Suo, Z.G., 2005. Stretchable interconnects for elastic electronic surfaces. Proc. IEEE 93 (8), 1459–1467.

Lanzara, G., Salowitz, N., Guo, Z.Q., Chang, F.K., 2010. A spider-web-like highly expandable sensor network for multifunctional materials. Adv. Mater. 22 (41), 4643–4648.

Leterrier, Y., Boogh, L., Andersons, J., Manson, J.A.E., 1997. Adhesion of silicon oxide layers on poly(ethylene terephthalate). 1. Effect of substrate properties on coating's fragmentation process. J. Polym. Sci. B Polym. Phys. 35 (9), 1449–1461.

Li, T., Suo, Z.G., Lacour, S.P., Wagner, S., 2005. Compliant thin film patterns of stiff materials as platforms for stretchable electronics. J. Mater. Res. 20 (12), 3274–3277.

Love, A.E.H., 2011. A Treatise on the Mathematical Theory of Elasticity. Dover Publications, New York, USA.

Lu, N., Kim, D.-H., 2013. Flexible and stretchable electronics paving the way for soft robotics. Soft Rob. 1 (P), 53–62.

Lu, N.S., Wang, X., Suo, Z., Vlassak, J., 2007. Metal films on polymer substrates stretched beyond 50%. Appl. Phys. Lett. 91 (22), 221909.

Meitl, M.A., Zhu, Z.T., Kumar, V., Lee, K.J., Feng, X., Huang, Y.Y., Adesida, I., Nuzzo, R.G., Rogers, J.A., 2006. Transfer printing by kinetic control of adhesion to an elastomeric stamp. Nat. Mater. 5 (1), 33–38.

Pijnenburg, K.G.W., Seelig, T., van der Giessen, E., 2005. Successively refined models for crack tip plasticity in polymer blends. Eur. J. Mech. – A/Solids 24 (5), 740–756.

Roguin, A., Grenadier, E., Peled, B., Markiewicz, W., Beyar, R., 1997. Acute and 30-day results of the serpentine balloon expandable stent implantation in simple and complex coronary arterial narrowings. Am. J. Cardiol. 80 (9), 1155–1162.

Sun, J.Y., Lu, N.S., Yoon, J., Oh, K.H., Suo, Z.G., Vlassak, J.J., 2012. Debonding and fracture of ceramic islands on polymer substrates. J. Appl. Phys. 111 (1).

Xu, S., Zhang, Y.H., Cho, J., Lee, J., Huang, X., Jia, L., Fan, J.A., Su, Y.W., Su, J., Zhang, H.G., Cheng, H.Y., Lu, B.W., Yu, C.J., Chuang, C., Kim, T.I., Song, T., Shigeta, K., Kang, S., Dagdeviren, C., Petrov, I., Braun, P.V., Huang, Y.G., Paik, U., Rogers, J.A., 2013. Stretchable batteries with self-similar serpentine interconnects and integrated wireless recharging systems. Nat. Commun. 4, 1543.

Yeo, W.-H., Kim, Y.-S., Lee, J., Ameen, A., Shi, L., Li, M., Wang, S., Ma, R., Jin, S.H., Kang, Z., Huang, Y., Rogers, J.A., 2013. Multi-functional electronics: multifunctional epidermal electronics printed directly onto the skin (Adv. Mater. 20/2013). Adv. Mater. 25 (20), 2772–2772.

Ying, M., Bonifas, A.P., Lu, N.S., Su, Y.W., Li, R., Cheng, H.Y., Ameen, A., Huang, Y.G., Rogers, J.A., 2012. Silicon nanomembranes for fingertip electronics. Nanotechnology 23 (34), 344004.

Yu, C.J., Duan, Z., Yuan, P.X., Li, Y.H., Su, Y.W., Zhang, X., Pan, Y.P., Dai, L.L., Nuzzo, R.G., Huang, Y.G., Jiang, H.Q., Rogers, J.A., 2013. Electronically programmable, reversible shape change in two- and three-dimensional hydrogel structures. Adv. Mater. 25 (11), 1541–1546.

Zhang, Y.H., Xu, S., Fu, H.R., Lee, J., Su, J., Hwang, K.C., Rogers, J.A., Huang, Y.G., 2013a. Buckling in serpentine microstructures and applications in elastomer-supported ultra-stretchable electronics with high areal coverage. Soft Matter 9 (33), 8062–8070.

Zhang, Y., Fu, H., Su, Y., Xu, S., Cheng, H., Fan, J.A., Hwang, K.-C., Rogers, J.A., Huang, Y., 2013b. Mechanics of ultra-stretchable self-similar serpentine interconnects. Acta Mater. 61 (20), 7816–7827.

Zhu, S., Huang, Y., Li, T., 2014. Extremely compliant and highly stretchable patterned graphene. Appl. Phys. Lett. 104 (17).